

Generalizable and Relightable Gaussian Splatting for Human Novel View Synthesis

Yipengjing Sun¹, Shengping Zhang^{*,1}, Chenyang Wang¹, Shunyuan Zheng¹, Zonglin Li¹, Xiangyang Ji²

¹Harbin Institute of Technology ²Tsinghua University

{yipengjing.sun, c.wang}@stu.hit.edu.cn, {sawyer0503, zonglin.li, s.zhang}@hit.edu.cn

xyji@tsinghua.edu.cn

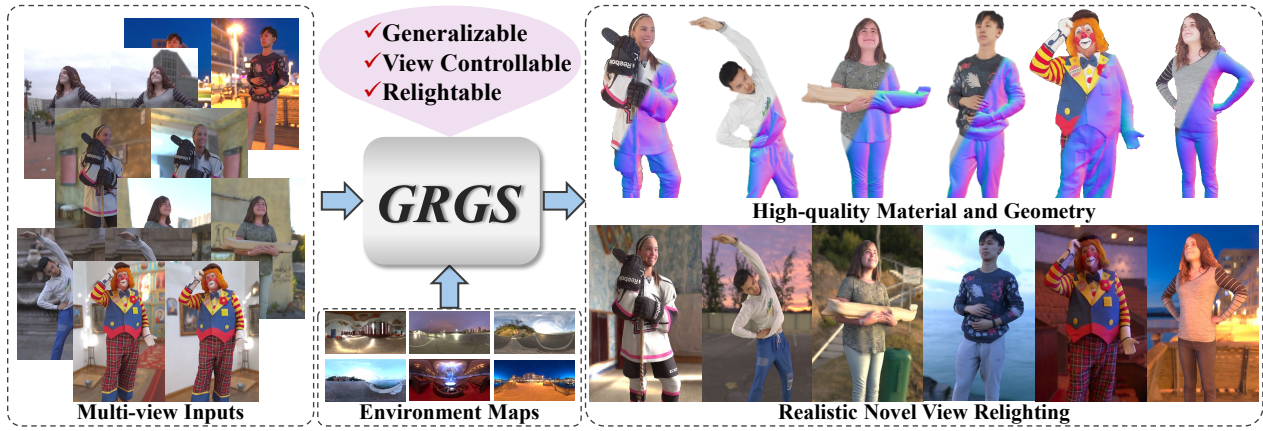


Figure 1. Given multi-view inputs and environment maps, GRGS reconstructs generalizable 3D representations with high-quality geometry and material while supporting realistic relighting rendering from arbitrary viewpoints.

Abstract

We propose GRGS, a generalizable and relightable 3D Gaussian framework for high-fidelity human novel view synthesis under diverse lighting conditions. Unlike existing methods that rely on per-character optimization or ignore physical constraints, GRGS adopts a feed-forward, fully supervised strategy projecting geometry, material, and illumination cues from multi-view 2D observations into 3D Gaussian representations. To recover accurate geometry under diverse lighting conditions, we introduce a Lighting-robust Geometry Refinement (LGR) module trained on synthetically relit data to predict precise depth and surface normals. Based on the high-quality geometry, a Physically Grounded Neural Rendering (PGNR) module is further proposed to integrate neural prediction with physics-based shading, supporting editable relighting with shadows and indirect illumination. Moreover, we design a 2D-to-3D projection training scheme leveraging differentiable supervision from ambient occlusion, direct, and indirect lighting maps, alleviating the computational cost of ray tracing. Extensive experiments demonstrate that GRGS achieves superior visual quality, geometric consistency, and generalization across

characters and lighting conditions. The project webpage is available at <https://sypj-98.github.io/grgs/>.

1. Introduction

Human novel view synthesis (NVS) aims to produce photorealistic images of human performers under a specific targeting novel viewpoint, which has a wide range of applications such as immersive telepresence, cinematic production, and AR/VR. To further improve realism and fidelity, relightable rendering, which enables editing lighting during synthesizing novel views, has become an important improvement over traditional NVS, as lighting significantly affects surface appearance and immersive shading. Although significant efforts have been devoted to developing effective relightable rendering, it is still a challenging task due to complex light transport in 3D space.

Prior methods [10, 14, 17, 26] typically rely on mesh-based geometry and texture reconstruction to support plausible viewpoint transitions, but they often involve complex reconstruction pipelines and struggle with generating accurate and smooth mesh surfaces, limiting their effectiveness for realistic relighting without extensive post-processing. Recent advances [23, 32, 37] in neural representations

* Corresponding author.

have substantially propelled the field of NVS. Specifically, NeRF-based approaches [8, 20, 27, 43, 58, 59, 65] incorporate physically-based rendering (PBR) principles into volumetric radiance fields or signed distance fields (SDFs) for implicit geometry and material encoding, enabling the synthesis of photorealistic images under novel viewpoints and lighting conditions. However, these methods typically require time-consuming per-character optimization and incur high computational costs, resulting in limited rendering speeds that hinder their practicality in real-world applications. Recently, 3D Gaussian Splatting (3DGS) [23] has emerged as an efficient and explicit neural representation, offering a fast training and inference process while maintaining high visual fidelity. To adapt 3DGS for relighting tasks, researchers [13, 19, 28, 29, 54] augment each 3D Gaussian point with intrinsic properties (geometry and appearance) and employ inverse rendering techniques to estimate light transport. Unfortunately, it remains reliant on iterative inverse rendering pipelines that are inherently ill-posed, resulting in inaccurate estimation of geometry and materials, which degrades the overall rendering quality. Moreover, per-character optimization still prevents them from being applied to relighting applications that require generalization across different characters.

In contrast to 3D methods, 2D image-based relighting approaches employ encoder-decoder architectures (*e.g.*, U-Net) [18, 24, 35, 38] or diffusion models [40, 41, 63] to learn lighting priors from large-scale relighting datasets, producing high-quality relit images under novel illumination in a generalized manner. Despite their efficiency and strong generalization capabilities, the lack of 3D consistent constraints makes 2D image-based methods suffer from flickering artifacts when rendering from precisely user-controlled viewpoints. In addition, although these methods often produce visually impressive relighting results, they often overlook physical interpretability as they entirely rely on neural networks to implicitly capture physical constraints.

To address these challenges, we propose GRGS, as shown in Fig. 1, a generalizable and relightable 3D Gaussian framework for high-fidelity human novel view synthesis under various lighting conditions by integrating multiple intrinsic attribute priors into 3D Gaussian representations. Unlike existing 3DGS-based methods that apply person-specific optimization, the core idea of GRGS is to adopt a supervised, data-driven strategy that learns to project geometry, material, and illumination cues from multi-view 2D observations onto 3D Gaussian attributes in a feed-forward manner for robust generalization and realistic relighting. Our framework starts by presenting a Lighting-robust Geometry Refinement (LGR) module, which first estimates coarse depth using a stereo-based method and then refines per-Gaussian surface normals to capture smooth and fine-grained details. To obtain reliable geometry under chal-

lenging illumination, we synthesize large-scale relit multi-view data, enabling LGR to produce geometry consistent across diverse lighting conditions, thereby mitigating feature mismatches and improving geometric accuracy. The refined geometric priors not only support realistic relighting but also serve as a critical bridge between the 2D image space and the 3D Gaussian domain, facilitating accurate positioning of Gaussians. With the geometry established, we design a Physically Grounded Neural Rendering (PGNR) module that integrates physics-based rendering with neural rendering, which synthesizes realistic shading phenomena, including shadows and indirect lighting, while enforcing physically grounded lighting consistency. PGNR employs geometry-aware decoders to infer Gaussian parameters and intrinsic attributes from the refined geometry in a feed-forward manner. In parallel, a lightweight encoder-decoder processes the high-resolution environment map to estimate direct illumination scaling factors and spherical harmonic coefficients for modeling indirect lighting. By incorporating a physically-based rendering, our framework ensures physically consistent light transport, achieving high-quality and photorealistic relighting results. Besides, the 2D-to-3D project strategy alleviates the computational cost of explicit ray tracing for visibility and global illumination, ensuring high efficiency during inference. In summary, our method makes the following key contributions:

- We propose GRGS, a generalizable and relightable 3D Gaussian framework that projects geometry, material, and illumination cues from multi-view 2D observations onto 3D Gaussian attributes in a feed-forward manner, enabling realistic and robust novel view synthesis of unseen data under novel lighting conditions.
- We present a Lighting-robust Geometry Refinement module trained on synthetically relit multi-view data to estimate accurate depth and surface normals, effectively mitigating geometry errors caused by uneven illumination.
- We design a Physically Grounded Neural Rendering module that combines physics-based rendering with neural rendering, achieving high-quality shading effects with improved computational efficiency.

2. Related Work

Person-specific human relighting. Traditional methods [6, 10–12, 14, 15, 52, 53] propose to sample the reflectance field of a human performer through a LightStage setup comprising controlled lighting systems and dense camera arrays, which can generate photorealistic renderings under novel lighting environments. However, the costly setup and complex person-specific relighting process constrain their widespread applications. With the rapid progress in neural implicit representations [1, 2, 33, 37, 47, 55, 56], neural inverse rendering [3, 4, 20, 43, 59, 61, 62, 65] has emerged as a promising approach for person-specific

human relighting, enabling the joint recovery of geometry, material, and illumination from multi-view images captured under arbitrary lighting conditions. Recent variants [7, 8, 28, 30, 45, 50, 57] extend inverse rendering to dynamic performers by integrating a parametric human body template into the learning of implicit fields, enabling temporally coherent reconstruction under varying poses and motions. However, these methods typically require time-consuming person-specific optimization and incur high computational costs, resulting in limited training and rendering speeds. With the advent of explicit point-based 3DGS [23] representation, recent 3DGS-based inverse rendering methods [13, 16, 19, 29, 54] explore the disentanglement of material, geometry, and lighting through the use of Gaussian points, enabling efficient training and fast inference. ARGS [28] pioneers the integration of animatable 3D Gaussians and inverse rendering, delivering visually compelling and relightable full-body human avatars. RGCA [42] leverages dynamic relighting data captured in a LightStage and an explicit mesh template to achieve high-quality relightable head avatars. However, such methods typically rely on time-consuming person-specific optimization. Moreover, performing inverse rendering from multi-view images under arbitrary illumination is inherently ill-posed, making it particularly difficult to accurately disentangle geometry, material, and lighting, ultimately limiting the fidelity of the final relighting results.

Generalizable human relighting. With the advancement of deep learning, data-driven methods [35, 38, 44, 51, 67] have achieved impressive results in portrait relighting from a single image, primarily by leveraging convolutional neural networks trained on synthetic data derived from OLAT datasets. However, these methods typically overlook underlying human geometry, leading to physically implausible light–shadow interactions. Recent efforts [18, 36] attempt to address this limitation by estimating human geometry, but monocular predictions remain insufficiently accurate for reliable relighting. Other approaches [22, 25, 46] attempt to learn light transport directly from 2D shading images. However, modeling complex 3D light transport in 2D space remains fundamentally challenging. Such methods are generally restricted to approximating low-frequency lighting effects and fail to generalize to unseen illumination. SwitchLight [24] circumvents the need for explicit 3D geometry by introducing physics-based rendering in the image domain, achieving high-quality relighting results. Nevertheless, the absence of an explicit 3D representation limits its ability to handle occlusions and maintain spatial consistency. More recently, diffusion-based generative models [40, 41, 63] demonstrate impressive relighting performance by leveraging strong pre-trained priors and high-quality lighting datasets, producing visually striking results

with high generalization ability. However, priors learned from pre-training and Light Stage supervision lack physics-based constraints during training, which in turn reduces the physical interpretability and realism of the outputs.

3. Method

As illustrated in Fig. 2, our proposed GRGS achieves generalizable and relightable human novel view synthesis via two core modules: (1) Lighting-robust Geometry Refinement (LGR) module and (2) Physically Grounded Neural Rendering (PGNR) module. The core idea is to adopt a supervised, data-driven strategy that projects intrinsic attributes from multi-view 2D observations onto 3D Gaussian representations in a feed-forward manner. Specifically, given a set of sparse-view human images, GRGS first constructs the LGR module to estimate depth using a stereo-based method and then refines per-Gaussian surface normals via a depth-aware refinement, which allows GRGS to mitigate geometry errors caused by uneven illumination (Sec. 3.1). Next, building on this accurate geometry, the PGNR module fuses physics-based rendering with neural rendering to synthesize realistic relighting phenomena. It leverages geometry-aware decoders for Gaussian parameters and intrinsic attributes, and incorporates environment map encoding to predict direct illumination scaling factors and spherical harmonic coefficients for modeling indirect illumination (Sec. 3.2). To ensure strong generalization and realistic rendering, we introduce a 2D-to-3D projection training strategy that reasonably transfers 2D illumination cues into the 3D Gaussian space, simultaneously improving rendering efficiency (Sec. 3.3).

3.1. Lighting-robust Geometry Refinement

To enable a generalizable and relightable 3D Gaussian framework, fast and accurate geometry reconstruction of the target performer is a critical foundation. This geometry not only determines the center of each Gaussian point but also serves as an essential component for the subsequent relighting stage. However, existing methods [13, 19, 29, 54] typically require per-scene training to optimize Gaussian centers and still struggle to guarantee high-quality and consistent geometry under various lighting. To address this challenge, we design a Lighting-robust Geometry Refinement module, consisting of stereo-based depth estimation and depth-guided normal refinement, which jointly produce accurate geometry robust to illumination changes.

Stereo-based Depth Estimation. Inspired by the generalization strategy of GPS-Gaussian [66], we leverage RAFT-Stereo [31], a stereo-based depth estimator that uses disparity as a geometric constraint across views, enabling consistent depth prediction and improved generalization

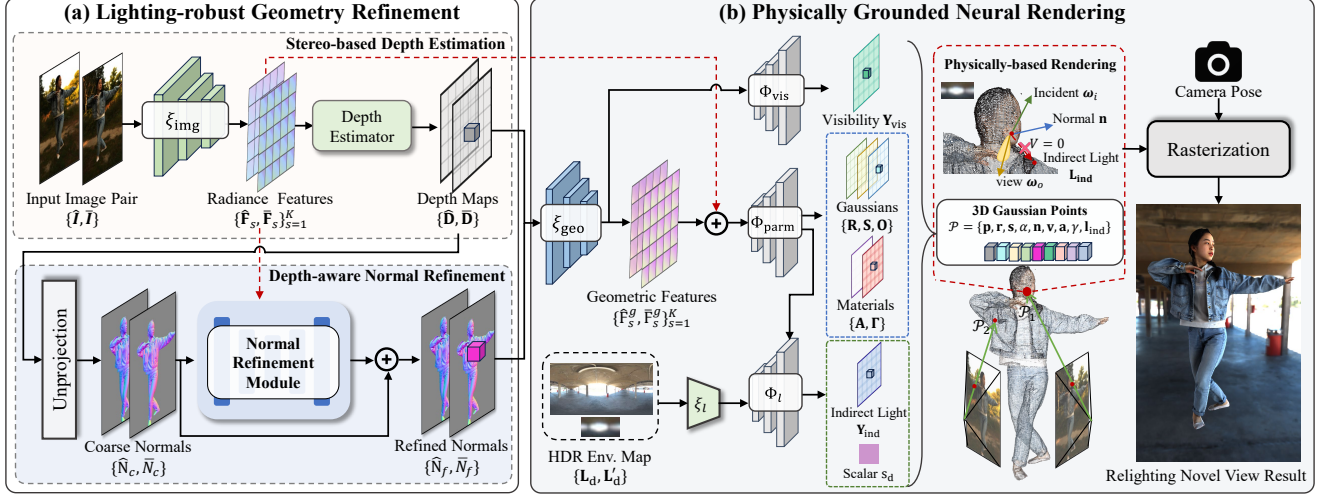


Figure 2. **Overview of GRGS.** Given sparse-view images of a performer under arbitrary illumination, GRGS first leverages the LGR module to reconstruct accurate depth and surface normals, and then employs the PGNR module for material decomposition and physically plausible relighting from novel viewpoints.

in diverse human-centric scenarios. However, pretrained depth estimators tend to be sensitive to illumination variations, leading to unreliable geometry estimation as shown in Fig 3. Therefore, we construct an image encoder trained by a large-scale multi-view relit dataset comprising hundreds of high-quality human scans, enabling the network to learn robust reflectance features for accurate depth estimation across diverse lighting conditions.

Specifically, given N sparse-view images $\{\mathbf{I}_i\}_{i=1}^N$ ($\mathbf{I}_i \in \mathbb{R}^{H \times W \times 3}$), captured under an arbitrary lighting of a human-centered scene, we select the two source views nearest to the target camera pose, denoted as $\{\hat{\mathbf{I}}, \bar{\mathbf{I}}\}$, as input for stereo rectification [39]. The rectified image pair is then passed through a shared lighting-robust feature extractor ξ_{img} , which is trained on the relit dataset encompassing diverse and varying illumination conditions to explicitly learn features invariant to lighting changes. This yields multi-scale radiance features $\{\hat{\mathbf{F}}_s, \bar{\mathbf{F}}_s\}_{s=1}^K$, where $\hat{\mathbf{F}}_s, \bar{\mathbf{F}}_s \in \mathbb{R}^{\frac{H}{2^s} \times \frac{W}{2^s} \times C}$ denote the feature representations at the s -th scale corresponding to the two input images $\{\hat{\mathbf{I}}, \bar{\mathbf{I}}\}$, respectively, and K is the total number of scales.

The radiance features mitigate lighting-induced feature mismatches to facilitate accurate depth estimation, as demonstrated in Sec. 4.2, while guiding the inference of geometry, material, and light transport within the 3D Gaussian representation (Sec. 3.2).

To balance memory efficiency in 3D correlation construction with rich semantic representation, we feed the final-scale image features $\{\hat{\mathbf{F}}_K, \bar{\mathbf{F}}_K\}$ and their corresponding camera parameters $\{\hat{\mathbf{G}}, \bar{\mathbf{G}}\}$ into a depth estimation module \mathcal{G} to predict full-resolution depth maps $\hat{\mathbf{D}}, \bar{\mathbf{D}} \in \mathbb{R}^{H \times W}$ for the selected source view images $\hat{\mathbf{I}}$ and $\bar{\mathbf{I}}$:

$$\langle \hat{\mathbf{D}}, \bar{\mathbf{D}} \rangle = \mathcal{G}(\hat{\mathbf{F}}_K, \bar{\mathbf{F}}_K, \hat{\mathbf{G}}, \bar{\mathbf{G}}) \quad (1)$$

Within \mathcal{G} , a low-resolution 3D correlation volume $\mathcal{M} \in \mathbb{R}^{\frac{H}{2^K} \times \frac{W}{2^K} \times \frac{W}{2^K}}$ is constructed:

$$\mathcal{M}_{ijk} = \sum_{l=1}^C (\hat{\mathbf{F}}_K)_{ijl} \cdot (\bar{\mathbf{F}}_K)_{ikl} \quad (2)$$

A GRU-based module is then employed iteratively to predict and refine down-sampled depth maps by querying the correlation volume \mathcal{M} . Finally, full-resolution, pixel-aligned depth maps are recovered by applying convex upsampling to the refined low-resolution predictions, ensuring spatial consistency and boundary preservation.

Depth-aware Normal Refinement. Although the depth map enables 3D point cloud reconstruction via unprojection, they do not capture surface normals, which are critical for accurate shading computations in Sec. 3.2. To fully harness the depth for surface orientation estimation, we first compute coarse surface normals reconstructed from spatial gradients of a single-view depth map $\mathbf{D} \in \mathbb{R}^{H \times W}$. Given a foreground pixel (u, v) of \mathbf{D} , its corresponding 3D point $\mathbf{X}(u, v) \in \mathbb{R}^3$ is obtained by unprojecting the depth value using the camera projection matrix $\mathbf{P} \in \mathbb{R}^{3 \times 4}$:

$$\mathbf{X}(u, v) = \Pi_{\mathbf{P}}(u, v, \mathbf{D}(u, v)) \quad (3)$$

where $\Pi_{\mathbf{P}}$ is an unprojection operator defined by \mathbf{P} . Next, a coarse normal map \mathbf{N}_c is computed via the normalized cross product of horizontal and vertical spatial gradients of the 3D position map \mathbf{X} :

$$\mathbf{N}_c(u, v) = \frac{(\mathbf{X}(u+1, v) - \mathbf{X}(u, v)) \times (\mathbf{X}(u, v+1) - \mathbf{X}(u, v))}{\|(\mathbf{X}(u+1, v) - \mathbf{X}(u, v)) \times (\mathbf{X}(u, v+1) - \mathbf{X}(u, v))\|} \quad (4)$$

where \times denotes the cross product. Due to the convex upsampling, the resulting depth maps lack high-frequency

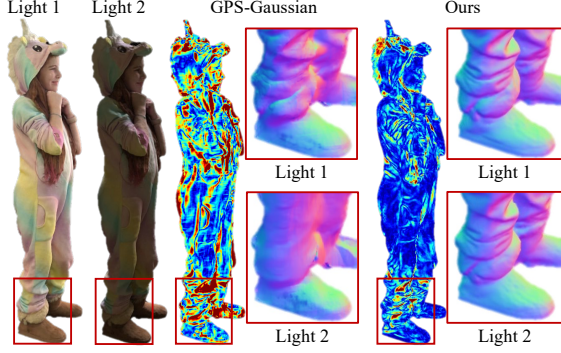


Figure 3. **Geometry consistency comparison between GRGS and GPS-Gaussian under varying illumination.** We visualize the normal difference heatmap, where cold colors indicate small angular deviations and hot colors denote large ones. GPS-Gaussian exhibits noticeable degradation under extreme lighting.

geometric details and exhibit checkerboard artifacts, as illustrated in Sec. 4.2. To address this, we introduce a normal refinement module \mathcal{N} based on a lightweight U-Net architecture, which leverages multi-scale radiance features $\{\mathbf{F}_s\}_{s=1}^K$ and coarse normals \mathbf{N}_c to predict normal offsets $\Delta\mathbf{N} \in \mathbb{R}^3$ and recover fine-grained surface details. The refinement process can be defined as

$$\Delta\mathbf{N} = \mathcal{N}(\mathbf{N}_c, \{\mathbf{F}_s\}_{s=1}^K) \quad (5)$$

The refined normal map \mathbf{N}_f is computed by normalizing the sum of \mathbf{N}_c and $\Delta\mathbf{N}$:

$$\mathbf{N}_f = \frac{\mathbf{N}_c + \Delta\mathbf{N}}{\|\mathbf{N}_c + \Delta\mathbf{N}\|} \quad (6)$$

We denote the normal maps of the two selected source views as $\hat{\mathbf{N}}_f$ and $\bar{\mathbf{N}}_f$.

3.2. Physically Grounded Neural Rendering

Based on the accurate geometry, we further propose a PGNR module to combine the generalization capabilities of neural networks with the physical accuracy of physically based rendering, enabling efficient inference of material properties and complex illumination of unseen data.

Geometry-aware Gaussian Parameter Regression. To support relightable rendering, PGNR parameterizes each 3D Gaussian point \mathcal{P} as a set of attributes: (1) vanilla attributes: position $\mathbf{p} \in \mathbb{R}^3$, rotation $\mathbf{r} \in \mathbb{R}^4$, scale $\mathbf{s} \in \mathbb{R}^3$, and opacity $\alpha \in \mathbb{R}$, (2) geometry-related attributes: surface normal $\mathbf{n} \in \mathbb{R}^3$ and light visibility $\mathbf{v} \in \mathbb{R}^{16}$ encoded via SH coefficients, (3) material attributes: albedo $\mathbf{a} \in \mathbb{R}^3$ and roughness $\gamma \in \mathbb{R}$, and (4) illumination attributes: indirect lighting $\mathbf{l}_{\text{ind}} \in \mathbb{R}^{48}$ represented by SH coefficients. We formulate these 3D attributes on corresponding 2D maps via pixel-aligned depth maps (Sec. 3.1), enabling direct inference of Gaussian point clouds without optimization. For

simplicity, we consider a single-view depth map \mathbf{D} and compute 3D position map \mathbf{X} via unprojection (Eq. 3), while normals \mathbf{N}_f are predicted by the refinement module. We introduce a geometry-aware encoder ξ_{geo} that extracts multi-scale geometric features $\{\mathbf{F}_s^g\}_{s=1}^K$ from \mathbf{D} and \mathbf{N}_f , encoding both 2D image features and 3D spatial geometry. These features are then fused with radiance features to incorporate appearance and geometric context for jointly modeling geometry-aware attribute maps. Specifically, we first extract the full-resolution Gaussian features Θ through a decoder Φ_{parm} :

$$\Theta = \Phi_{\text{parm}}(\{\mathbf{F}_s\}_{s=1}^K \oplus \{\mathbf{F}_s^g\}_{s=1}^K) \quad (7)$$

where \oplus denotes the concatenation operation applied across all feature levels. Subsequently, the vanilla Gaussian parameter maps (rotation map \mathbf{R} , scale map \mathbf{S} , and opacity map \mathbf{O}) are predicted with a Gaussian head h_g :

$$\langle \mathbf{R}, \mathbf{S}, \mathbf{O} \rangle = h_g(\Theta) \quad (8)$$

For material attributes, we introduce a residual component $\Delta\mathbf{A}$ to accelerate the convergence of albedo estimation under diverse lighting conditions. This component acts as a delighting term, helping disentangle shadows and illumination effects from the intrinsic surface properties. We achieve this by leveraging a material prediction head h_m to jointly estimate the residual albedo $\Delta\mathbf{A}$ and the surface roughness map Γ :

$$\langle \Delta\mathbf{A}, \Gamma \rangle = h_m(\Theta) \quad (9)$$

The final albedo is computed as: $\mathbf{A} = \text{Sigmoid}(\mathbf{I} + \Delta\mathbf{A})$, where \mathbf{I} denotes the input image. Besides, since the SH-encoded visibility map \mathbf{Y}_{vis} is independent of image appearance, we predict it via another lightweight decoder Φ_{vis} conditioned solely on the geometric features $\{\mathbf{F}_s^g\}_{s=1}^K$.

Light Parameterization. Accurate shading in 3D space typically requires dense sampling of incoming light directions, leading to substantial computational and memory overhead. To mitigate this, we prefilter the high-resolution HDR environment map $\mathbf{L}_d \in \mathbb{R}^{H_h \times W_h \times 3}$ to obtain a convolved version $\mathbf{L}'_d \in \mathbb{R}^{H_i \times W_i \times 3}$ that approximates the integral of incident illumination:

$$\mathbf{L}'_d(\omega') = \int_{\Omega} (\omega' \cdot \omega)^l \mathbf{L}_d(\omega) d\omega \quad (10)$$

where ω and ω' denote spherical directions in the original and convolved environment map respectively, Ω represents the unit sphere, and l is the shininess exponent controlling the angular falloff in the Phong reflectance model. However, such integration may result in underexposed lighting compared to ground-truth shading, as illustrated in Sec. 4.2. To address this, we introduce a direct illumination scaling



Figure 4. Qualitative comparison of our method and 3DGS-based methods. Zoom in for the best view.

factor $s_d \in \mathbb{R}$ to globally compensate for the brightness discrepancy. In addition, since the SH-encoded indirect lighting map \mathbf{Y}_{ind} is influenced not only by the appearance and geometry but also by the input illumination, we design a light encoder-decoder that predicts the direct illumination scaling map \mathbf{S}_d and the indirect lighting map \mathbf{Y}_{ind} :

$$\langle \mathbf{S}_d, \mathbf{Y}_{\text{ind}} \rangle = h_l (\Phi_l (\xi_l (\mathbf{L}_d) \oplus \mathbf{L}'_d) \oplus \Theta) \quad (11)$$

where ξ_l , Φ_l , and h_l denote the light encoder, decoder, and output head, respectively. Then, s_d is obtained by spatially averaging \mathbf{S}_d over the foreground N_f :

$$s_d = \frac{\sum_{i=1}^{N_f} \mathbf{S}_d (u_i, v_i)}{N_f} \quad (12)$$

Physically-based Rendering. To enable physically plausible light interaction on the human surface, we compute

the PBR color \mathbf{C}_{PBR} for each Gaussian point. Following the rendering equation [21], the outgoing radiance \mathbf{C}_{PBR} in direction ω_o can be given by:

$$\mathbf{C}_{\text{PBR}}(\omega_o) = \int_{\Omega} \mathbf{L}(\omega_i) f(\omega_i, \omega_o, \mathbf{a}, \gamma) (\omega_i \cdot \mathbf{n}) d\omega_i \quad (13)$$

where f is the simplified Disney BRDF function [5] modeling the surface reflectance properties, and Ω here represents the hemisphere oriented around the surface normal \mathbf{n} . $\mathbf{L}(\omega_i)$ denotes the incident radiance from direction ω_i :

$$\mathbf{L}(\omega_i) = V(\omega_i) (s_d \mathbf{L}'_d(\omega_i)) + (1 - V(\omega_i)) \mathbf{L}_{\text{ind}}(\omega_i) \quad (14)$$

where $V(\omega_i)$ denotes the light visibility from direction ω_i , parameterized using SH coefficients \mathbf{v} . Similarly, $\mathbf{L}_{\text{ind}}(\omega_i)$ represents the indirect illumination from direction ω_i , also encoded via SH coefficients \mathbf{l}_{ind} . Although R3DGS [13] employs a similar lighting model, it estimates indirect il-

lumination in an implicit manner through unsupervised inverse rendering, which often results in inaccurate predictions and limited generalization to novel lighting conditions while imposing a substantial computational burden due to the explicit ray tracing strategy. In contrast, our GRGS utilizes the strong generalization capability of a U-Net-based architecture in conjunction with a 2D-to-3D projection training strategy, enabling more accurate estimation of both visibility and indirect illumination under arbitrary lighting conditions. After computing the physically-based rendering color \mathbf{C}_{PBR} for each Gaussian point, we perform rasterization to synthesize the final image.

3.3. 2D-to-3D Projection Training

Leveraging the excellent differentiability of 3DGS [23], GRGS optimizes lighting parameters in the 3D space directly from 2D image supervision, thereby circumventing the costly computation of explicit ray tracing. Specifically, ground truths of ambient occlusion, direct lighting, and indirect lighting maps are used as photometric supervision signals to guide the optimization of the 3D Gaussian representation via efficient gradient-based learning. Among these signals, ambient occlusion and direct lighting maps are jointly used to provide more accurate supervision for visibility estimation. While ambient occlusion captures geometric occlusion effects, direct lighting offers complementary shadow-related illumination cues, and their combination helps enforce visibility consistency between 2D renderings and the underlying 3D geometry. For effective indirect lighting learning within the rendering equation, we employ a gradient-truncated hard shadow fusion scheme, which truncates gradients through visibility to prevent erroneous gradient propagation and leverages hard shadow fusion to accelerate the convergence of indirect lighting.

4. Experiments

Implementation Details. Our framework is trained on a single NVIDIA RTX 4090 GPU over approximately four days. We first train the LGR module for 100K iterations, where both the human subject and illumination conditions are randomly sampled in each iteration. Next, we train the entire framework for 300K iterations to jointly optimize for high-quality geometry reconstruction and realistic relighting performance. More details of the optimization process are provided in Supp.Mat..

Datasets. We utilize two human scan datasets, Twindom [48] and THuman2.0 [60], to validate the effectiveness of our method. To ensure high-quality rendering, we carefully selected 800 scans from Twindom and 337 scans from THuman2.0, filtering out meshes with noticeable artifacts. Additionally, 384 HDR environment maps were collected from Polyhaven, HDRMAPS, and iHDRI to simulate



Figure 5. Qualitative comparison between our method and 2D image-based approaches. The bottom row shows results from the real dataset [66]. Zoom in for the best view.

diverse illumination conditions. More dataset construction details are listed in Supp.Mat.. In addition, we also employ multi-view real-world data from GPS-Gaussian [66] and DNA-Rendering [9] to further evaluate the generalization ability of our method in real scenarios.

Baselines and Metrics. We compare our method on our synthetic dataset and real dataset [66] against two 3DGS-based approaches, R3DGS [13] and ARGS [28], as well as two 2D image-based methods, IC-Light [63] and SwitchLight [24]. Note that since 2D methods cannot synthesize novel views, we directly use ground-truth novel view images as their input for a fair comparison. For quantitative evaluation, we employ PSNR, SSIM, and LPIPS to evaluate the diffuse albedo, ambient occlusion, and relighting quality. Further, we utilize MAE to evaluate the normal map.

4.1. Comparison Results

We first make a comparison with 3D-based methods (*i.e.*, R3DGS [13] and ARGS [28]) from the perspective of material estimation, geometry reconstruction, and relighting quality, as shown in Fig. 4 and Table 1. R3DGS [13] struggles to recover smooth, detailed normals from sparse views without human-specific priors, leading to suboptimal relighting performance. ARGS [28] alleviates this by introducing a body template prior. However, optimizing geometry solely from rendered images leads to overly smooth surfaces lacking high-frequency details. Moreover, both methods depend on inverse rendering under an inherently ill-posed formulation, which yields inaccurate material estimation and consequently degrades the overall quality of relighting results. Thanks to the proposed LGR and PGNR modules, GRGS produces high-quality geometry and realistic relighting results under novel viewpoints.

Furthermore, a comparison with representative 2D-based relighting methods (*i.e.*, IC-Light [63] and SwitchLight [24]) is illustrated in Fig. 5. The baseline meth-

Table 1. **Quantitative comparison on the synthetic dataset.** In accordance with [66], the SSIM and LPIPS metrics are calculated within the bounding box delineating the human region, while the MAE of normal and PSNR metrics is computed within the foreground mask.

	Normal MAE↓	Diffuse Albedo			Ambient Occlusion			Relighting		
	PSNR↑	SSIM↑	LPIPS↓	PSNR↑	SSIM↑	LPIPS↓	PSNR↑	SSIM↑	LPIPS↓	
R3DGS [13]	10.208	23.584	0.829	0.165	20.983	0.761	0.388	21.983	0.812	0.162
ARGs [28]	6.941	25.937	0.865	0.142	23.721	0.837	0.129	23.879	0.846	0.147
Ours	5.369	27.536	0.936	0.080	24.470	0.865	0.105	27.977	0.926	0.099

ods produce noticeable shading and lighting variations that often lack physical plausibility, exhibiting artifacts such as inconsistent light–geometry interactions and unnatural shadow orientations, thereby diminishing overall realism. In contrast, our results closely match the ground-truth images generated by a physically-based renderer and deliver superior perceptual quality. Additional evidence is provided by a user study (see Supp.Mat.).



Figure 6. Enhanced novel view rendering and surface normals results via LGR. Zoom in for the best view.

4.2. Ablation Study

Geometry reconstruction. A major limitation of the original GPS-Gaussian [66] is that it struggles to maintain robustness against uneven lighting on the human surface without lighting priors, leading to a significant degradation in geometric consistency, as shown in Fig. 3. In contrast, our LGR module learns lighting-robust radiance features under diverse illumination conditions, thereby improving reconstruction accuracy under uneven lighting and enhancing both geometric consistency and NVS quality (Table. 2).

Although the lighting-robust radiance features enhance depth estimation accuracy, the use of convex upsampling for full-resolution recovery inevitably causes the loss of high-frequency geometric details and introduces checkerboard artifacts in the coarse normal map N_c , as shown in Fig. 6. The proposed normal refinement module leverages both se-

mantic information from radiance features and geometric cues from the coarse normal map to reconstruct high-quality surface normals with consistent improvements in qualitative (Fig. 6) and quantitative (see Supp.Mat.) results.

Table 2. NVS and Depth Evaluation.

Method	NVS			Depth	
	PSNR↑	SSIM↑	LPIPS↓	EPE↓	1 pix↑
GPS-Gaussian [66]	30.444	0.913	0.107	1.463	68.91
Ours	31.694	0.949	0.067	0.692	85.39

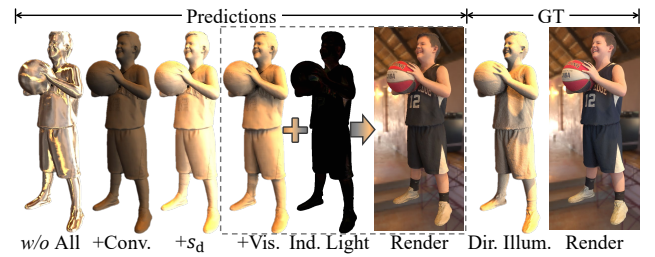


Figure 7. Enhanced light transport through PGNR. Zoom in for the best view.

Light Transport. To mitigate the brightness loss caused by convolved environment lighting, we introduce a feed-forward direct illumination scaling factor s_d , which yields shading closer to the ground truth as shown in Fig. 7. To further enhance realism by modeling shadow effects and complex light interactions such as multi-bounce illumination, we additionally learn light visibility and indirect lighting. As illustrated in the figure, our method accurately captures occlusion shadows from the arm and ball. Across all experiments, realistic effects are achieved with only tens of light samples per Gaussian. Specifically, sampling 40 rays strikes an effective balance between quality and efficiency. With TensorRT acceleration, our model runs at 20 FPS during inference. Further analysis of computational efficiency is provided in Supp.Mat..

5. Conclusion

This paper proposes GRGS, a generalizable and relightable 3D Gaussian framework for high-fidelity human novel view synthesis under diverse lighting conditions. GRGS adopts a supervised 2D-to-3D projection strategy to transfer geometry, material, and illumination cues from multi-view 2D

observations into 3D Gaussian attributes, enabling efficient feed-forward inference without person-specific optimization. To ensure accurate geometry, we first construct a Lighting-robust Geometry Refinement module to estimate robust depth and surface normals. In addition, a Physically Grounded Neural Rendering module is presented to integrate physics-based shading with neural inference to synthesize realistic lighting effects, avoiding the cost of explicit ray tracing. Thanks to these designs, GRGS achieves high-quality, editable human relighting and strong generalization to unseen identities and lighting environments.

References

- [1] Kara-Ali Aliev, Artem Sevastopolsky, Maria Kolos, Dmitry Ulyanov, and Victor Lempitsky. Neural point-based graphics. In *Computer Vision–ECCV 2020: 16th European Conference, Glasgow, UK, August 23–28, 2020, Proceedings, Part XXII 16*, pages 696–712. Springer, 2020. [2](#)
- [2] Sai Bi, Zexiang Xu, Kalyan Sunkavalli, David Kriegman, and Ravi Ramamoorthi. Deep 3d capture: Geometry and reflectance from sparse multi-view images. In *Proceedings of the IEEE/CVF conference on computer vision and pattern recognition*, pages 5960–5969, 2020. [2](#)
- [3] Mark Boss, Raphael Braun, Varun Jampani, Jonathan T Barron, Ce Liu, and Hendrik Lensch. Nerd: Neural reflectance decomposition from image collections. In *Proceedings of the IEEE/CVF International Conference on Computer Vision*, pages 12684–12694, 2021. [2](#)
- [4] Mark Boss, Varun Jampani, Raphael Braun, Ce Liu, Jonathan Barron, and Hendrik Lensch. Neural-pil: Neural pre-integrated lighting for reflectance decomposition. *Advances in Neural Information Processing Systems*, 34: 10691–10704, 2021. [2](#)
- [5] Brent Burley and Walt Disney Animation Studios. Physically-based shading at disney. In *Acm Siggraph*, pages 1–7. vol. 2012, 2012. [6](#), [1](#)
- [6] Charles-Félix Chabert, Per Einarsson, Andrew Jones, Bruce Lamond, Wan-Chun Ma, Sebastian Sylwan, Tim Hawkins, and Paul Debevec. Relighting human locomotion with flowed reflectance fields. In *ACM SIGGRAPH 2006 Sketches*, pages 76–es. 2006. [2](#)
- [7] Yushuo Chen, Zerong Zheng, Zhe Li, Chao Xu, and Yebin Liu. Meshavatar: Learning high-quality triangular human avatars from multi-view videos. *arXiv preprint arXiv:2407.08414*, 2024. [3](#)
- [8] Zhaoxi Chen and Ziwei Liu. Relighting4d: Neural relightable human from videos. In *European conference on computer vision*, pages 606–623. Springer, 2022. [2](#), [3](#)
- [9] Wei Cheng, Ruixiang Chen, Siming Fan, Wanqi Yin, Keyu Chen, Zhongang Cai, Jingbo Wang, Yang Gao, Zhengming Yu, Zhengyu Lin, et al. Dna-rendering: A diverse neural actor repository for high-fidelity human-centric rendering. In *Proceedings of the IEEE/CVF International Conference on Computer Vision*, pages 19982–19993, 2023. [7](#), [8](#), [10](#)
- [10] Paul Debevec. The light stages and their applications to photoreal digital actors. *SIGGRAPH Asia*, 2(4):1–6, 2012. [1](#), [2](#)
- [11] Paul Debevec, Tim Hawkins, Chris Tchou, Haarm-Pieter Duiker, Westley Sarokin, and Mark Sagar. Acquiring the reflectance field of a human face. In *Proceedings of the 27th annual conference on Computer graphics and interactive techniques*, pages 145–156, 2000.
- [12] Paul Debevec, Andreas Wenger, Chris Tchou, Andrew Gardner, Jamie Waese, and Tim Hawkins. A lighting reproduction approach to live-action compositing. *ACM Transactions on Graphics (TOG)*, 21(3):547–556, 2002. [2](#)
- [13] Jian Gao, Chun Gu, Youtian Lin, Zhihao Li, Hao Zhu, Xun Cao, Li Zhang, and Yao Yao. Relightable 3d gaussians: Realistic point cloud relighting with brdf decomposition and ray tracing. In *European Conference on Computer Vision*, pages 73–89. Springer, 2024. [2](#), [3](#), [6](#), [7](#), [8](#), [4](#), [5](#)
- [14] Kaiwen Guo, Peter Lincoln, Philip Davidson, Jay Busch, Xueming Yu, Matt Whalen, Geoff Harvey, Sergio Orts-Escalano, Rohit Pandey, Jason Dourgarian, et al. The relightables: Volumetric performance capture of humans with realistic relighting. *ACM Transactions on Graphics (ToG)*, 38(6):1–19, 2019. [1](#), [2](#)
- [15] Tim Hawkins, Jonathan Cohen, and Paul Debevec. A photometric approach to digitizing cultural artifacts. In *Proceedings of the 2001 conference on Virtual reality, archeology, and cultural heritage*, pages 333–342, 2001. [2](#)
- [16] Yu Hong, Yize Wu, Zhehao Shen, Chengcheng Guo, Yuheng Jiang, Yingliang Zhang, Qiang Hu, Jingyi Yu, and Lan Xu. Beam: Bridging physically-based rendering and gaussian modeling for relightable volumetric video. In *Proceedings of the 33rd ACM International Conference on Multimedia*, pages 7968–7977, 2025. [3](#)
- [17] James Imber, Jean-Yves Guillemaut, and Adrian Hilton. Intrinsic textures for relightable free-viewpoint video. In *Computer Vision–ECCV 2014: 13th European Conference, Zurich, Switzerland, September 6–12, 2014, Proceedings, Part II 13*, pages 392–407. Springer, 2014. [1](#)
- [18] Chaonan Ji, Tao Yu, Kaiwen Guo, Jingxin Liu, and Yebin Liu. Geometry-aware single-image full-body human relighting. In *European Conference on Computer Vision*, pages 388–405. Springer, 2022. [2](#), [3](#)
- [19] Yingwenqi Jiang, Jiadong Tu, Yuan Liu, Xifeng Gao, Xiaoxiao Long, Wenping Wang, and Yuexin Ma. Gaussian-shader: 3d gaussian splatting with shading functions for reflective surfaces. In *Proceedings of the IEEE/CVF Conference on Computer Vision and Pattern Recognition*, pages 5322–5332, 2024. [2](#), [3](#)
- [20] Haian Jin, Isabella Liu, Peijia Xu, Xiaoshuai Zhang, Songfang Han, Sai Bi, Xiaowei Zhou, Zexiang Xu, and Hao Su. Tensoir: Tensorial inverse rendering. In *Proceedings of the IEEE/CVF Conference on Computer Vision and Pattern Recognition*, pages 165–174, 2023. [2](#)
- [21] James T Kajiya. The rendering equation. In *Proceedings of the 13th annual conference on Computer graphics and interactive techniques*, pages 143–150, 1986. [6](#)
- [22] Yoshihiro Kanamori and Yuki Endo. Relighting humans: occlusion-aware inverse rendering for full-body human images. *arXiv preprint arXiv:1908.02714*, 2019. [3](#)

[23] Bernhard Kerbl, Georgios Kopanas, Thomas Leimkühler, and George Drettakis. 3d gaussian splatting for real-time radiance field rendering. *ACM Trans. Graph.*, 42(4):139–1, 2023. 1, 2, 3, 7

[24] Hoon Kim, Minje Jang, Wonjun Yoon, Jisoo Lee, Donghyun Na, and Sanghyun Woo. Switchlight: Co-design of physics-driven architecture and pre-training framework for human portrait relighting. In *Proceedings of the IEEE/CVF Conference on Computer Vision and Pattern Recognition*, pages 25096–25106, 2024. 2, 3, 7

[25] Manuel Lagunas, Xin Sun, Jimei Yang, Ruben Villegas, Jianming Zhang, Zhixin Shu, Belen Masia, and Diego Gutierrez. Single-image full-body human relighting. *arXiv preprint arXiv:2107.07259*, 2021. 3

[26] Guannan Li, Chenglei Wu, Carsten Stoll, Yebin Liu, Kiran Varanasi, Qionghai Dai, and Christian Theobalt. Capturing relightable human performances under general uncontrolled illumination. In *Computer Graphics Forum*, pages 275–284. Wiley Online Library, 2013. 1

[27] Jia Li, Lu Wang, Lei Zhang, and Beibei Wang. Tensosdf: Roughness-aware tensorial representation for robust geometry and material reconstruction. *ACM Transactions on Graphics (TOG)*, 43(4):1–13, 2024. 2

[28] Zhe Li, Yipengjing Sun, Zerong Zheng, Lizhen Wang, Shengping Zhang, and Yebin Liu. Animatable and relightable gaussians for high-fidelity human avatar modeling. *arXiv preprint arXiv:2311.16096v4*, 2024. 2, 3, 7, 8, 4

[29] Zhihao Liang, Qi Zhang, Ying Feng, Ying Shan, and Kui Jia. Gs-ir: 3d gaussian splatting for inverse rendering. In *Proceedings of the IEEE/CVF Conference on Computer Vision and Pattern Recognition*, pages 21644–21653, 2024. 2, 3

[30] Wenbin Lin, Chengwei Zheng, Jun-Hai Yong, and Feng Xu. Relightable and animatable neural avatars from videos. In *Proceedings of the AAAI Conference on Artificial Intelligence*, pages 3486–3494, 2024. 3

[31] Lahav Lipson, Zachary Teed, and Jia Deng. Raft-stereo: Multilevel recurrent field transforms for stereo matching. In *2021 International Conference on 3D Vision (3DV)*, pages 218–227. IEEE, 2021. 3, 4

[32] Stephen Lombardi, Tomas Simon, Jason Saragih, Gabriel Schwartz, Andreas Lehrmann, and Yaser Sheikh. Neural volumes: Learning dynamic renderable volumes from images. *ACM Trans. Graph.*, 38(4):65:1–65:14, 2019. 1

[33] Stephen Lombardi, Tomas Simon, Jason Saragih, Gabriel Schwartz, Andreas Lehrmann, and Yaser Sheikh. Neural volumes: Learning dynamic renderable volumes from images. *arXiv preprint arXiv:1906.07751*, 2019. 2

[34] Ilya Loshchilov and Frank Hutter. Decoupled weight decay regularization. In *International Conference on Learning Representations*, 2017. 1

[35] Yiqun Mei, He Zhang, Xuaner Zhang, Jianming Zhang, Zhixin Shu, Yilin Wang, Zijun Wei, Shi Yan, HyunJoon Jung, and Vishal M Patel. Lightpainter: Interactive portrait relighting with freehand scribble. In *Proceedings of the IEEE/CVF conference on computer vision and pattern recognition*, pages 195–205, 2023. 2, 3

[36] Abhimitra Meka, Rohit Pandey, Christian Haene, Sergio Orts-Escalano, Peter Barnum, Philip David-Son, Daniel Erickson, Yinda Zhang, Jonathan Taylor, Sofien Bouaziz, et al. Deep relightable textures: volumetric performance capture with neural rendering. *ACM Transactions on Graphics (TOG)*, 39(6):1–21, 2020. 3

[37] Ben Mildenhall, Pratul P Srinivasan, Matthew Tancik, Jonathan T Barron, Ravi Ramamoorthi, and Ren Ng. Nerf: Representing scenes as neural radiance fields for view synthesis. *Communications of the ACM*, 65(1):99–106, 2021. 1, 2

[38] Rohit Pandey, Sergio Orts-Escalano, Chloe Legendre, Christian Haene, Sofien Bouaziz, Christoph Rhemann, Paul E Debevec, and Sean Ryan Fanello. Total relighting: learning to relight portraits for background replacement. *ACM Trans. Graph.*, 40(4):43–1, 2021. 2, 3

[39] Demetrios V Papadimitriou and Tim J Dennis. Epipolar line estimation and rectification for stereo image pairs. *IEEE transactions on image processing*, 5(4):672–676, 1996. 4

[40] Puntawat Ponglerapakorn, Nontawat Tritrong, and Supasorn Suwajanakorn. Difareli: Diffusion face relighting. In *Proceedings of the IEEE/CVF international conference on computer vision*, pages 22646–22657, 2023. 2, 3

[41] Mengwei Ren, Wei Xiong, Jae Shin Yoon, Zhixin Shu, Jianming Zhang, HyunJoon Jung, Guido Gerig, and He Zhang. Relightful harmonization: Lighting-aware portrait background replacement. In *Proceedings of the IEEE/CVF Conference on Computer Vision and Pattern Recognition*, pages 6452–6462, 2024. 2, 3

[42] Shunsuke Saito, Gabriel Schwartz, Tomas Simon, Junxuan Li, and Giljoo Nam. Relightable gaussian codec avatars. In *Proceedings of the IEEE/CVF conference on computer vision and pattern recognition*, pages 130–141, 2024. 3

[43] Pratul P Srinivasan, Boyang Deng, Xiuming Zhang, Matthew Tancik, Ben Mildenhall, and Jonathan T Barron. Nerv: Neural reflectance and visibility fields for relighting and view synthesis. In *Proceedings of the IEEE/CVF Conference on Computer Vision and Pattern Recognition*, pages 7495–7504, 2021. 2

[44] Tiancheng Sun, Jonathan T Barron, Yun-Ta Tsai, Zexiang Xu, Xueming Yu, Graham Fyffe, Christoph Rhemann, Jay Busch, Paul E Debevec, and Ravi Ramamoorthi. Single image portrait relighting. *ACM Trans. Graph.*, 38(4):79–1, 2019. 3

[45] Wenzhang Sun, Yunlong Che, Han Huang, and Yandong Guo. Neural reconstruction of relightable human model from monocular video. In *Proceedings of the IEEE/CVF International Conference on Computer Vision*, pages 397–407, 2023. 3

[46] Daichi Tajima, Yoshihiro Kanamori, and Yuki Endo. Relighting humans in the wild: Monocular full-body human relighting with domain adaptation. In *Computer Graphics Forum*, pages 205–216. Wiley Online Library, 2021. 3

[47] Justus Thies, Michael Zollhöfer, and Matthias Nießner. Deferred neural rendering: Image synthesis using neural textures. *Acm Transactions on Graphics (TOG)*, 38(4):1–12, 2019. 2

[48] Twindom, 2020. <https://web.twindom.com>. 7, 1

[49] Jianyuan Wang, Minghao Chen, Nikita Karaev, Andrea Vedaldi, Christian Rupprecht, and David Novotny. Vggt: Visual geometry grounded transformer. In *Proceedings of the Computer Vision and Pattern Recognition Conference*, pages 5294–5306, 2025. 5

[50] Shaofei Wang, Bozidar Antic, Andreas Geiger, and Siyu Tang. Intrinsicavatar: Physically based inverse rendering of dynamic humans from monocular videos via explicit ray tracing. In *Proceedings of the IEEE/CVF Conference on Computer Vision and Pattern Recognition*, pages 1877–1888, 2024. 3

[51] Zhibo Wang, Xin Yu, Ming Lu, Quan Wang, Chen Qian, and Feng Xu. Single image portrait relighting via explicit multiple reflectance channel modeling. *ACM Transactions on Graphics (ToG)*, 39(6):1–13, 2020. 3

[52] Andreas Wenger, Andrew Gardner, Chris Tchou, Jonas Unger, Tim Hawkins, and Paul Debevec. Performance relighting and reflectance transformation with time-multiplexed illumination. *ACM Transactions on Graphics (ToG)*, 24(3):756–764, 2005. 2

[53] Tim Weyrich, Wojciech Matusik, Hanspeter Pfister, Bernd Bickel, Craig Donner, Chien Tu, Janet McAndless, Jinho Lee, Addy Ngan, Henrik Wann Jensen, et al. Analysis of human faces using a measurement-based skin reflectance model. *ACM Transactions on Graphics (ToG)*, 25(3):1013–1024, 2006. 2

[54] Tong Wu, Jia-Mu Sun, Yu-Kun Lai, Yuwen Ma, Leif Kobbelt, and Lin Gao. Deferredgs: Decoupled and relightable gaussian splatting with deferred shading. *IEEE Transactions on Pattern Analysis and Machine Intelligence*, 2025. 2, 3

[55] Zexiang Xu, Kalyan Sunkavalli, Sunil Hadap, and Ravi Ramamoorthi. Deep image-based relighting from optimal sparse samples. *ACM Transactions on Graphics (ToG)*, 37(4):1–13, 2018. 2

[56] Zexiang Xu, Sai Bi, Kalyan Sunkavalli, Sunil Hadap, Hao Su, and Ravi Ramamoorthi. Deep view synthesis from sparse photometric images. *ACM Transactions on Graphics (ToG)*, 38(4):1–13, 2019. 2

[57] Zhen Xu, Sida Peng, Chen Geng, Linzhan Mou, Zihan Yan, Jiaming Sun, Hujun Bao, and Xiaowei Zhou. Relightable and animatable neural avatar from sparse-view video. *arXiv preprint arXiv:2308.07903*, 2023. 3

[58] Zhen Xu, Sida Peng, Chen Geng, Linzhan Mou, Zihan Yan, Jiaming Sun, Hujun Bao, and Xiaowei Zhou. Relightable and animatable neural avatar from sparse-view video. In *Proceedings of the IEEE/CVF Conference on Computer Vision and Pattern Recognition*, pages 990–1000, 2024. 2

[59] Yao Yao, Jingyang Zhang, Jingbo Liu, Yihang Qu, Tian Fang, David McKinnon, Yanghai Tsin, and Long Quan. Neilf: Neural incident light field for physically-based material estimation. In *European Conference on Computer Vision*, pages 700–716. Springer, 2022. 2

[60] Tao Yu, Zerong Zheng, Kaiwen Guo, Pengpeng Liu, Qionghai Dai, and Yebin Liu. Function4d: Real-time human volumetric capture from very sparse consumer rgbd sensors. In *Proceedings of the IEEE/CVF conference on computer vision and pattern recognition*, pages 5746–5756, 2021. 7, 1

[61] Jingyang Zhang, Yao Yao, Shiwei Li, Jingbo Liu, Tian Fang, David McKinnon, Yanghai Tsin, and Long Quan. Neilf++: Inter-reflectable light fields for geometry and material estimation. In *Proceedings of the IEEE/CVF International Conference on Computer Vision*, pages 3601–3610, 2023. 2

[62] Kai Zhang, Fujun Luan, Qianqian Wang, Kavita Bala, and Noah Snavely. Physg: Inverse rendering with spherical gaussians for physics-based material editing and relighting. In *Proceedings of the IEEE/CVF Conference on Computer Vision and Pattern Recognition*, pages 5453–5462, 2021. 2

[63] Lvmin Zhang, Anyi Rao, and Maneesh Agrawala. Scaling in-the-wild training for diffusion-based illumination harmonization and editing by imposing consistent light transport. In *The Thirteenth International Conference on Learning Representations*, 2025. 2, 3, 7

[64] Richard Zhang, Phillip Isola, Alexei A Efros, Eli Shechtman, and Oliver Wang. The unreasonable effectiveness of deep features as a perceptual metric. In *Proceedings of the IEEE conference on computer vision and pattern recognition*, pages 586–595, 2018. 4

[65] Xiuming Zhang, Pratul P Srinivasan, Boyang Deng, Paul Debevec, William T Freeman, and Jonathan T Barron. Nerfactor: Neural factorization of shape and reflectance under an unknown illumination. *ACM Transactions on Graphics (ToG)*, 40(6):1–18, 2021. 2

[66] Shunyuan Zheng, Boyao Zhou, Ruizhi Shao, Boning Liu, Shengping Zhang, Liqiang Nie, and Yebin Liu. Gps-gaussian: Generalizable pixel-wise 3d gaussian splatting for real-time human novel view synthesis. In *Proceedings of the IEEE/CVF conference on computer vision and pattern recognition*, pages 19680–19690, 2024. 3, 7, 8, 1, 4, 6, 9

[67] Hao Zhou, Sunil Hadap, Kalyan Sunkavalli, and David W Jacobs. Deep single-image portrait relighting. In *Proceedings of the IEEE/CVF international conference on computer vision*, pages 7194–7202, 2019. 3

[68] Matthias Zwicker, Hanspeter Pfister, Jeroen Van Baar, and Markus Gross. Surface splatting. In *Proceedings of the 28th annual conference on Computer graphics and interactive techniques*, pages 371–378, 2001. 1

Generalizable and Relightable Gaussian Splatting for Human Novel View Synthesis

Supplementary Material

In this supplementary material, we provide additional information, including preliminary concepts (Sec.6), implementation details (Sec.7), more comparison results (Sec.8), more analysis on core component (Sec.9), detailed loss functions (Sec.10) and a discussion of limitations (Sec. 11).

6. Preliminary

3D Gaussian Splatting. 3DGS [23] is an explicit point-based representation that models a scene as a set of 3D Gaussians. Each Gaussian is parameterized by its position \mathbf{p} , a covariance matrix Σ (constructed from a rotation vector \mathbf{r} and a scale vector \mathbf{s}), opacity α , and color \mathbf{c} . In our framework, the color \mathbf{c} can be formulated to represent any attribute requiring optimization under 2D-to-3D supervision. Then each gaussian can be expressed as:

$$f(\mathbf{x}|\mathbf{p}, \Sigma) = \exp\left(-\frac{1}{2}(\mathbf{x} - \mathbf{p})^\top \Sigma^{-1}(\mathbf{x} - \mathbf{p})\right) \quad (15)$$

where the constant factor in Eq. 15 is omitted. A 2D image is rendered through rasterization. Specifically, the 3D Gaussians are projected onto 2D planes, resulting in 2D Gaussians. The pixel color \mathbf{C} is determined by blending N ordered 2D Gaussians that overlap this pixel:

$$\mathbf{C} = \sum_{i=1}^N \alpha_i \prod_{j=1}^{i-1} (1 - \alpha_j) \mathbf{c}_i \quad (16)$$

where \mathbf{c}_i is the color of each 2D Gaussian, and α_i is the blending weight derived from the learned opacity and 2D Gaussian distribution [68].

BRDF modelling. The whole BRDF [5] employed in our method is composed of a diffuse term f_d and a specular term f_s , defined as:

$$f(\omega_i, \omega_o, \mathbf{a}, \gamma) = \underbrace{\frac{\mathbf{a}}{\pi}}_{f_d} + \underbrace{\frac{D(\mathbf{h}; \gamma)F(\omega_o, \mathbf{h})G(\omega_i, \omega_o, \mathbf{h}; \gamma)}{(\omega_i \mathbf{n}) \cdot (\omega_o \mathbf{n})}}_{f_s} \quad (17)$$

where $\mathbf{h} = \frac{(\omega_i + \omega_o)}{2}$ denotes the half-vector between the incoming direction ω_i and outgoing direction ω_o . The functions $D(\cdot)$, $F(\cdot)$, and $G(\cdot)$ correspond to the normal distribution function (NDF), Fresnel term, and geometric term, respectively. The parameter \mathbf{a} represents the albedo, while γ denotes the roughness.

7. Implementation Details

Dataset construction. We construct our dataset following a similar multi-view setup as GPS-Gaussian [66], but unlike GPS-Gaussian, which only renders novel view RGB images, our data construction explicitly accounts for geometry, material, and illumination information. We employ Cycles renderer in Blender to render the datasets, positioning 16 cameras uniformly in a circular arrangement with an angular interval of 22.5° between adjacent cameras. Each human scan is rendered from every input camera pair, along with three novel views sampled from the intersection arc between the input cameras, under five randomly selected HDR environment maps. For each rendering, we generate corresponding outputs, including albedo, normal, depth, foreground mask, ambient occlusion, indirect light, shading, and relighting images. Since the scans are captured under uniformly illuminated conditions, their texture maps are approximately treated as intrinsic albedo in this dataset. Our training set consists of 600 scans from the Twindom [48] dataset and 277 scans from the THuman2.0 [60] dataset. For evaluation, we reserve 200 scans from Twindom and 60 scans from THuman2.0 as the test set.

Network Architecture and Hyperparameter. The detailed network architecture is illustrated in Fig. 8. In the LGR module, we set the number of radiance feature scales $K = 3$, with feature dimensions of 32, 48, and 96, respectively, for $\{\mathbf{F}_s\}_{s=1}^K$. In the PGNR module, the target environment map is convolved from a resolution of 1024×512 down to 32×16 using a shininess exponent of $l = 16$. Owing to the efficient light parameterization, we sample only 40 rays per Gaussian point oriented around the surface normal \mathbf{n} for PBR, enabling fast and high-quality shading under arbitrary environment maps. We train our GRGS framework using the AdamW [34] optimizer with an initial learning rate of $2e^{-4}$. For the LGR module, we use a batch size of 2, while a batch size of 1 is adopted for the PGNR module. Note that during PGNR training, the LGR module is jointly optimized to facilitate more accurate localization of Gaussian point positions.

8. More Comparison Results

Computation efficiency. To quantitatively validate the computational efficiency of our method, we conduct runtime and relighting comparisons between our spherical harmonics-based visibility (SH-Vis) modeling and ray-

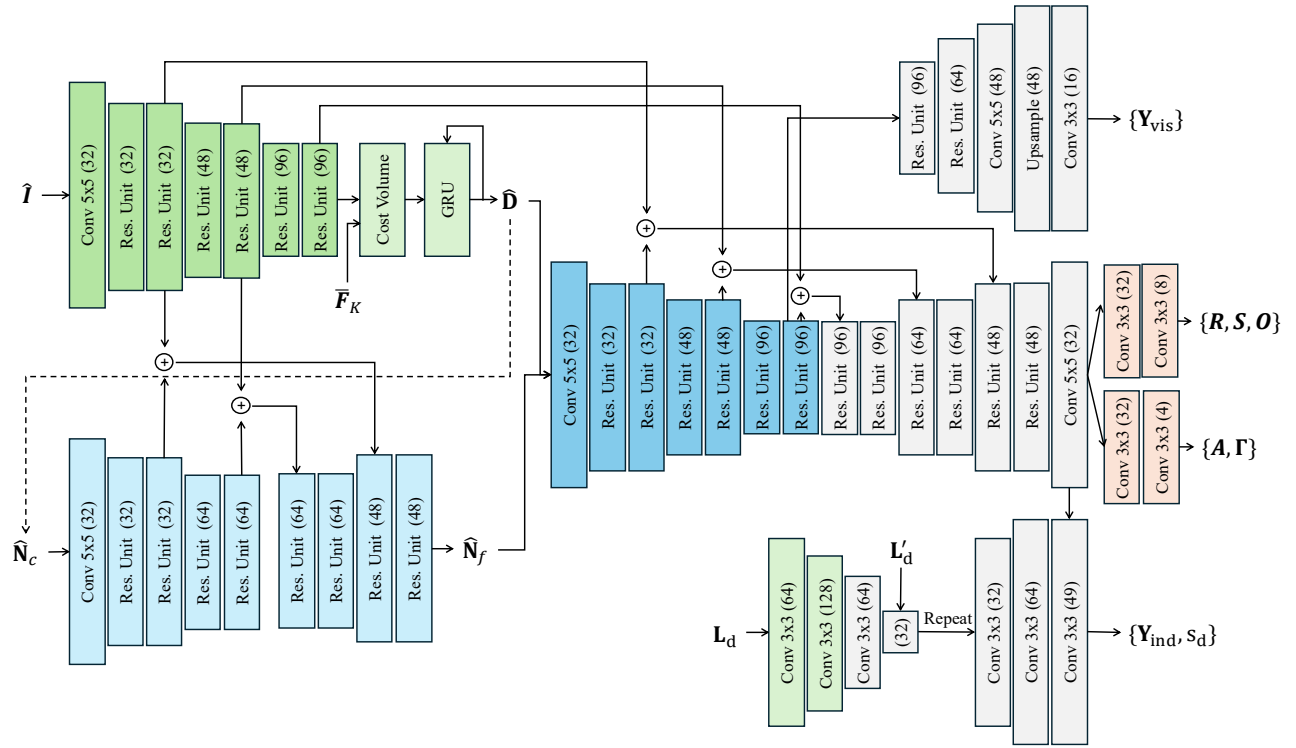


Figure 8. Network architecture. For simplicity, we consider a single-view image \hat{I} as the input, while \bar{F}_K denotes the final-scale image feature extracted from the other view.

Table 3. Runtime & relighting comparisons between spherical harmonics-based visibility (SH-Vis) modeling and ray-traced visibility (RT-Vis) under various ray sampling configurations.

Sampling No.	SH-Vis			RT-Vis		
	40	128	256	40	128	256
Runtime ↓	49	71	103	230	819	1536
Relit PSNR ↑	27.977	27.968	28.041	26.762	27.593	27.812

traced visibility (RT-Vis) proposed in R3DGS under various ray sampling configurations (40, 128, 256) as shown in Table 3. The results demonstrate that our SH-Vis design achieves a significant speedup (at least 4x faster), compared to ray-traced visibility, while also delivering better relighting quality. Although SH-Vis-256 yields slightly higher image quality, its runtime doubles compared to SH-Vis-40, which hinders real-time inference. Moreover, SH-Vis-40 achieves comparable PSNR due to effective light parametrization, making it a more practical choice for our experiments. In contrast, RT-Vis incurs substantially longer runtimes and yields lower relighting quality, primarily because Gaussian point clouds lack explicit surfaces, forcing ray tracing to rely on computationally expensive volumet-

Table 4. Runtime & relighting comparisons against 3D baselines.

Sampling NO.	Ours	R3DGS		ARGs	
	40	40	256	40	256
Runtime ↓	49	221	1480	1103	6318
Relit PSNR ↑	27.977	19.214	21.983	21.336	23.879

ric intersection, which is not yet as accurate or efficient as mesh-based methods. In comparison, SH-Vis can learn high-frequency details from ground truth supervision, enabling it to achieve more accurate and visually appealing relighting results.

Furthermore, we conduct runtime and relighting quality comparisons against 3D baselines in Table 4, including R3DGS and ARGS. R3DGS accelerates rendering by pre-computing visibility via ray tracing. To ensure a fair evaluation, we include this precomputation time in the total runtime. Specifically, we compare R3DGS and ARGS under two ray sampling configurations: 40 rays and 256 rays. The 256-ray setting is consistent with our main paper experiments, while the 40-ray setting is included to highlight efficiency under reduced sampling. Both R3DGS and ARGS compute visibility using ray tracing over 3D Gaussian point



Figure 9. Additional relighting results of various performers under diverse lighting conditions. Zoom in for the best view.

clouds. ARGS suffers from significantly slower rendering speed due to its heavy Style-Unet architecture. However, our method achieves superior relighting quality while being significantly more computationally efficient due to the SH-Vis and light parametrization.

User study. We conducted a user study to evaluate the visual plausibility of our method on the proposed test set. In

a pairwise comparison setup between our method and each baseline, 50 participants (including 40 students specializing in computer vision and graphics and 10 individuals from the general public) were asked to select the more visually convincing relighting result from each image pair. The study was conducted on 50 image samples. We report the preference rate (defined as the fraction of times participants favored our results over those of the baselines) in Table 5,

where participants consistently rated our relighting outputs as more visually convincing and physically coherent than those of baseline methods.

Table 5. User preference rate.

Methods	R3DGS	ARGS	IC-Light	SwitchLight
Preference rate	0.93	0.85	0.77	0.65

9. Further Analysis

Geometry reconstruction. Table 6 demonstrates the effectiveness of the proposed normal refinement module by evaluating surface normal quality using the MAE metric. While the incorporation of lighting-robust features facilitates the recovery of smooth normals, fine-grained geometric details remain lacking due to the limitations of convex upsampling. In contrast, our normal refinement module successfully captures high-frequency details, leading to improvements in MAE.

Table 6. MAE Comparison

Method	GPS-Gaussian [66]	Coarse Normal	Refined Normal
MAE ↓	8.145	5.903	5.369

Inference speed The end-to-end pipeline, including geometry reconstruction, material prediction, and relighting, runs at approximately 20 FPS on an RTX 4090 GPU. The runtime breakdown of each module is shown in Table 7.

More results. We present additional relighting results of various performers under diverse lighting conditions in Fig. 9. The photorealistic quality, lighting consistency, and physical plausibility observed in these results highlight the effectiveness and generalization of our proposed method.

Dynamic extension. Although GRGS is not explicitly designed with a temporal consistency module for dynamic scenarios, it can be extended to dynamic settings under uniform lighting conditions, as shown in Fig. 10, Fig. 11 and Fig. 12. By treating input images as diffuse albedo, the method mitigates most flickering artifacts caused by temporal inconsistencies. We further provide a qualitative comparison on dynamic sequences against R3DGS [13] and ARGS [28], as shown in Fig. 13 and Fig. 14. R3DGS struggles to reconstruct geometry from sparse-view inputs, resulting in severe artifacts in relighting. ARGS alleviates this issue by employing a body template, which improves geometric consistency. However, its template deformation

Table 7. Run time breakdown of each module.

Methods	Geometry	Gaussian attributes	Rendering	Total
Run time (ms)	11	21	17	49

capability is limited, making it difficult to handle loose or highly deformable clothing such as long dresses. Moreover, both approaches require extensive optimization, taking 3–4 days to process a 200-frame sequence, which restricts practicality.

In contrast, our method requires no extra optimization, achieves near real-time inference, and does not rely on body templates, enabling robust generalization to diverse human identities and clothing styles. With the proposed PGNR module, our approach further delivers more natural, coherent, and physically plausible relighting results across dynamic sequences.

10. Loss Functions

LGR loss. We supervise geometry reconstruction using a depth loss $\mathcal{L}_{\text{depth}}$ and a normal loss $\mathcal{L}_{\text{normal}}$, formulated as:

$$\mathcal{L}_{\text{LGR}} = \mathcal{L}_{\text{depth}} + \mathcal{L}_{\text{normal}} \quad (18)$$

The depth loss $\mathcal{L}_{\text{depth}}$ is defined as the weighted L1 distance between the predicted depth sequence $\{\mathbf{d}_1, \dots, \mathbf{d}_N\}$ and ground truth depth \mathbf{d}_{GT} with exponentially increasing weights following [31]:

$$\mathcal{L}_{\text{depth}} = \sum_{i=1}^N \mu^{N-i} \|\mathbf{d}_i - \mathbf{d}_{\text{GT}}\|_1 \quad (19)$$

where μ is set to 0.9. For the normal loss, given ground truth \mathbf{N}_{GT} , we combine the L1 distance and a perceptual loss [64] to ensure both geometric accuracy and surface smoothness:

$$\mathcal{L}_{\text{normal}} = \mathcal{L}_1(\mathbf{N}_f, \mathbf{N}_{\text{GT}}) + \lambda_1 \mathcal{L}_{\text{percep}}(\mathbf{N}_f, \mathbf{N}_{\text{GT}}) \quad (20)$$

PGNR loss. We define the overall loss as a combination of $\mathcal{L}_{\text{albedo}}$, material smoothness loss $\mathcal{L}_{\text{smooth}}$, light transport loss \mathcal{L}_{LT} , and PBR loss \mathcal{L}_{PBR} to facilitate appearance reconstruction and relighting via 2D-to-3D supervision:

$$\mathcal{L}_{\text{PGNR}} = \mathcal{L}_{\text{albedo}} + \mathcal{L}_{\text{smooth}} + \mathcal{L}_{\text{LT}} + \mathcal{L}_{\text{PBR}} \quad (21)$$

Note that after PBR and rasterization, the material maps: \mathbf{A} and \mathbf{F} ; the visibility V parameterized by SH map \mathbf{Y}_{vis} ; the indirect light \mathbf{L}_{ind} parameterized by SH map \mathbf{Y}_{ind} ; the direct light \mathbf{L}_d , and the PBR color \mathbf{C}_{PBR} are all rendered into the 2D image space as $\mathbf{I}_{\text{albedo}}$, $\mathbf{I}_{\text{rough}}$, \mathbf{I}_{ao} , \mathbf{I}_{ind} , \mathbf{I}_d and \mathbf{I}_{PBR} , respectively. Thus, they can be supervised via corresponding 2D ground truths. Specifically, the albedo loss is

composed of an L1 loss and a perceptual loss to measure the difference between the predicted albedo and the ground truth $\mathbf{I}'_{\text{albedo}}$:

$$\mathcal{L}_{\text{albedo}} = \mathcal{L}_1(\mathbf{I}_{\text{albedo}}, \mathbf{I}'_{\text{albedo}}) + \lambda_2 \mathcal{L}_{\text{percep}}(\mathbf{I}_{\text{albedo}}, \mathbf{I}'_{\text{albedo}}) \quad (22)$$

To promote spatially smooth material estimation, we adopt a bilateral smoothness loss following [13]:

$$\mathcal{L}_{\text{smooth}} = \lambda_3 \|\nabla \mathbf{I}_{\text{albedo}}\| \exp(-\|\nabla \mathbf{I}'_{\text{albedo}}\|) + \lambda_4 \|\nabla \mathbf{I}_{\text{rough}}\| \exp(-\|\nabla \mathbf{I}'_{\text{albedo}}\|) \quad (23)$$

Note that ground truth roughness maps are not available; thus, the roughness map Γ is learned implicitly through the entire PBR framework. The light transport loss is combined with ambient occlusion loss \mathcal{L}_{ao} , direct light loss \mathcal{L}_{d} , and indirect light loss \mathcal{L}_{ind} , we use L1 distance to measure the predicted and ground truth ones:

$$\mathcal{L}_{\text{LT}} = \mathcal{L}_1(\mathbf{I}_{\text{ao}}, \mathbf{I}'_{\text{ao}}) + \mathcal{L}_1(\mathbf{I}_{\text{dl}}, \mathbf{I}'_{\text{dl}}) + \mathcal{L}_1(\mathbf{I}_{\text{indl}}, \mathbf{I}'_{\text{indl}}) \quad (24)$$

The PBR loss applies an L1 loss and a perceptual loss for measuring the overall relighting quality:

$$\mathcal{L}_{\text{PBR}} = \mathcal{L}_1(\mathbf{I}_{\text{PBR}}, \mathbf{I}'_{\text{PBR}}) + \lambda_5 \mathcal{L}_1(\mathbf{I}_{\text{PBR}}, \mathbf{I}'_{\text{PBR}}) \quad (25)$$

The loss weights are set as follows: $\lambda_1 = 0.2$, $\lambda_2 = 0.2$, $\lambda_3 = 0.1$, $\lambda_4 = 0.1$, and $\lambda_5 = 0.2$.

11. Limitations

While our method achieves high-quality relighting results on human subjects, it has two primary limitations. First, due to the intrinsic constraints of the adopted rendering equation, our approach cannot accurately model transparent or metallic materials, such as eyeglasses and metallic sequins, and struggles with extremely thin structures, including individual hair strands. Future work could explore the integration of advanced reflectance models to further improve the realism of relighting.

Second, our method requires at least two input images with precise camera poses for stereo-based geometry estimation and relighting. This dependency on multi-view calibration limits its applicability in scenarios with unknown or imprecise poses and reduces robustness in unconstrained environments. In future work, we aim to incorporate geometry priors from foundational models, such as VGGT [49], enabling novel view synthesis and high-quality relighting from arbitrary viewpoints without explicit calibration.



Figure 10. Dynamic relighting case from GPS-Gaussian [66] under diverse lighting conditions and novel viewpoints.



Figure 11. Dynamic relighting case from DNA-Rendering [9] under diverse lighting conditions and novel viewpoints.



Figure 12. Dynamic relighting case from DNA-Rendering [9] under diverse lighting conditions and novel viewpoints.

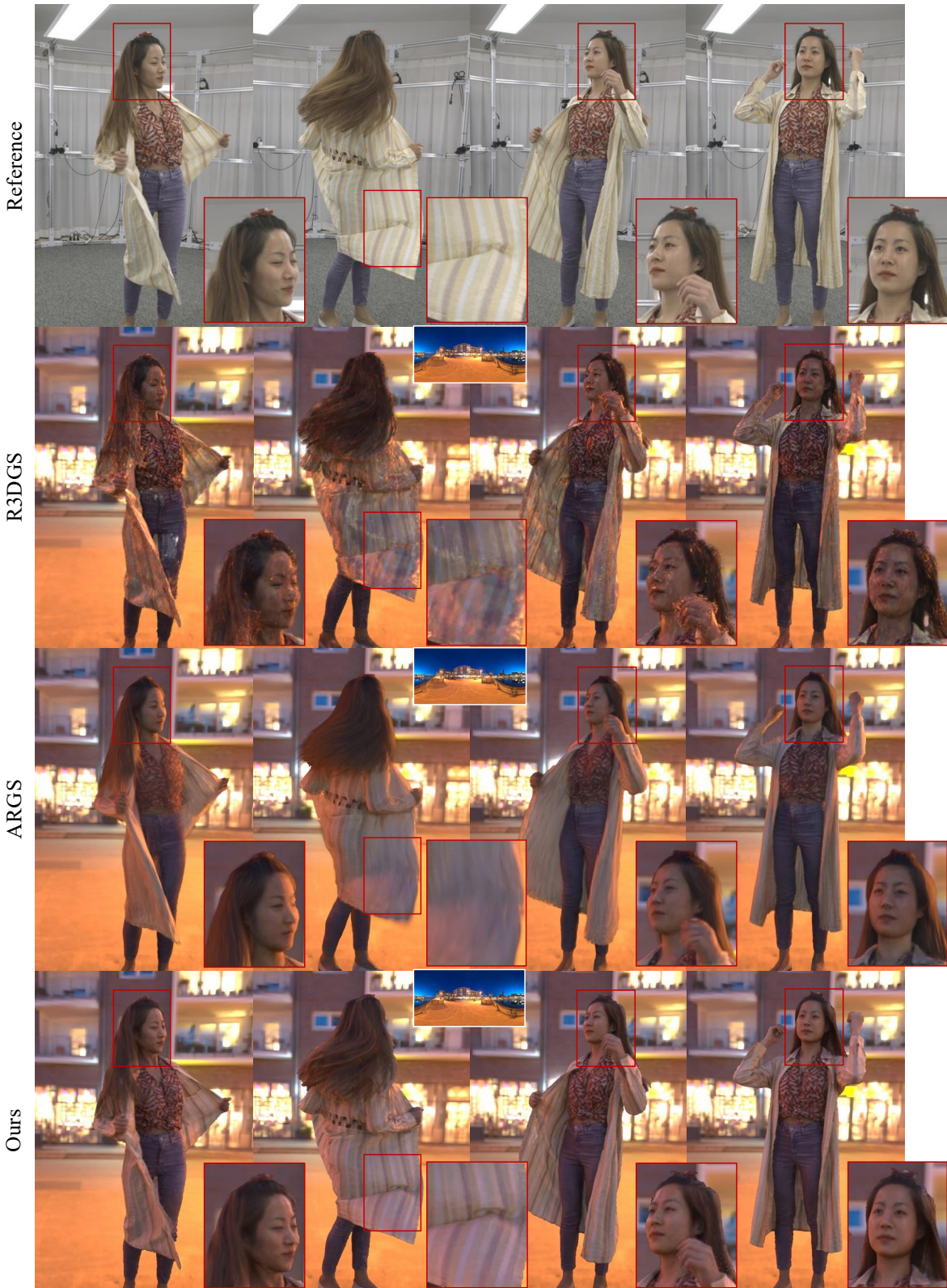


Figure 13. Dynamic relighting comparison on the GPS-Gaussian [66] dataset.

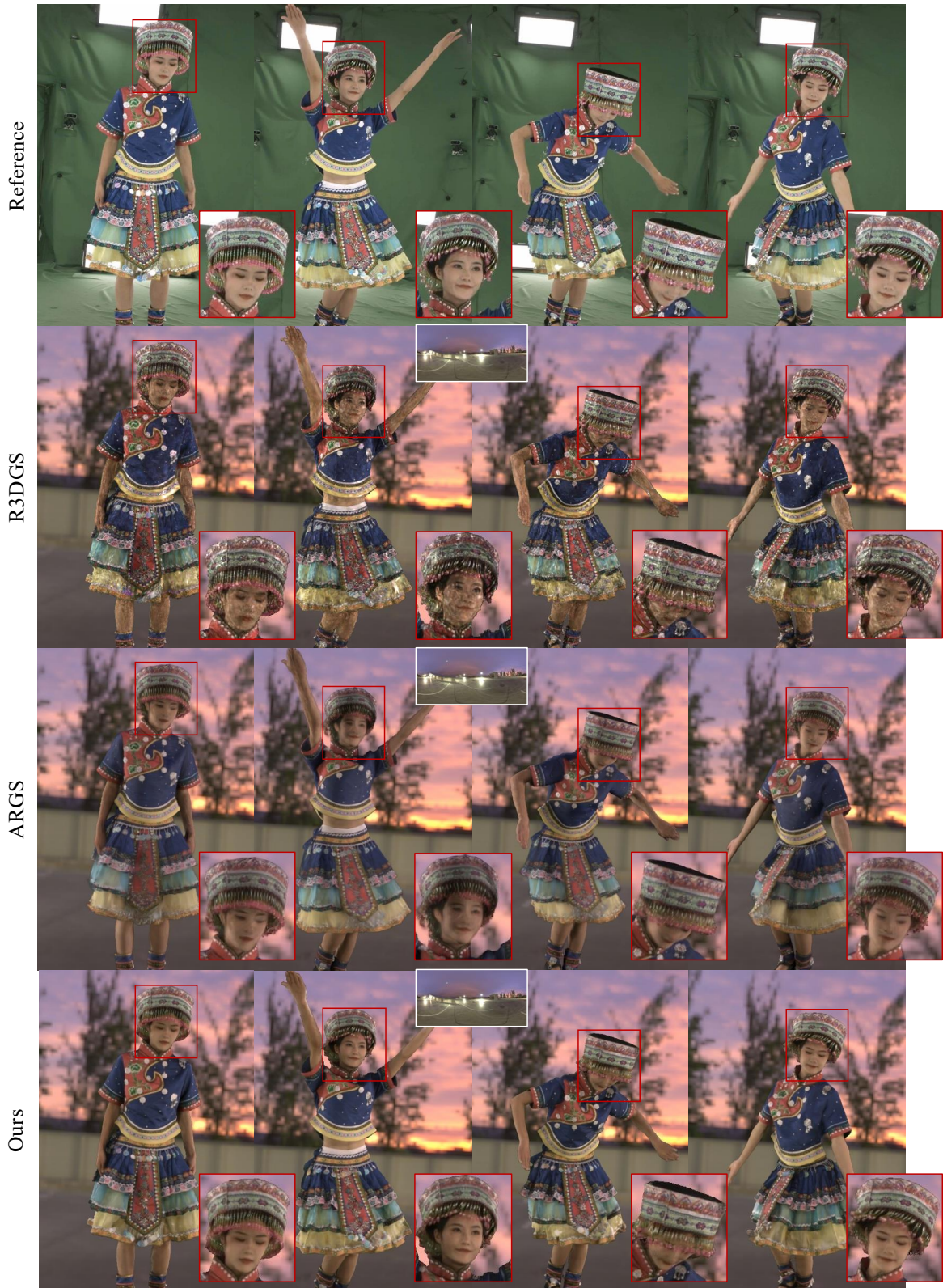


Figure 14. Dynamic relighting comparison on the DNA-Rendering [9] dataset.